



Cite this: DOI: 10.1039/d6eb00003g

Understanding the fast charging ability limitation in a graphite electrode for Li-ion batteries. Heterogeneities of lithiation in conventional electrodes

Corentin Renais,^a Marta Mirolo,^b Victor Vanpeene,^c Maxime Servajon,^a Jakub Drnec,^b Fannie Alloin^{id} *^a and Claire Villevieille^{id} *^a

Graphite electrodes dominate the Li-ion battery market as a negative electrode material. As a consequence, it is of utmost importance to understand the origin of their power limitation for fast charging applications in electric vehicles. We first investigated thick and porous graphite electrodes using rate capability tests by varying the electrode porosity and the salt concentration, showing a first correlation between porosity, salt concentration, and high-power capability. Using X-ray holo-tomography at large-scale facilities, we probed the microstructure of the electrodes, showing the increase of tortuosity as a function of porosity. These gathered results were strengthened by using *operando* vertical profile high resolution X-ray diffraction. Heterogeneities of lithiation along the electrode thickness were found by varying the electrode porosity and the cycling rate from C/4 to C/1. The highest tortuosity results in large ionic transport hindrance along the electrode thickness. The in-depth investigation demonstrated that larger heterogeneities through the electrode thickness are observed. These heterogeneities depend on the graphite reaction mechanisms and are more pronounced in the biphasic domain ascribed to the flat potential plateau. Finally, by correlating all the results, we were able to estimate the local current densities and demonstrate that the effective local C-rate can reach twice the applied C-rate, raising serious concerns about the ageing phenomenon in batteries.

Received 8th January 2026,
Accepted 9th April 2026

DOI: 10.1039/d6eb00003g

rsc.li/EESBatteries

Broader context

Fast-charging lithium-ion batteries are essential for the widespread adoption of electric vehicles and the efficient use of renewable energy, yet their electrochemical performance remains limited by a fundamental trade-off between energy and power density. This limitation is particularly true for graphite negative electrodes, which, despite their commercial use, exhibit strong rate limitations that can lead to non-uniform lithiation, accelerated ageing, and safety risks under high-power operation. While electrode engineering strategies such as calendaring and porosity optimisation are commonly employed to improve power performance, their impact on ion transport and reaction heterogeneity within working electrodes remains poorly understood. By combining electrochemical measurements, three-dimensional microstructural characterisation, and *operando* spatially resolved X-ray diffraction, this study directly links electrode microstructure to lithium-ion transport limitations and lithiation gradients in graphite electrodes. The results demonstrate that increased tortuosity in low-porosity electrodes leads to severe ionic transport limitations, heterogeneous current distribution, and local effective C-rates significantly exceeding the applied current. These findings highlight the critical role of three-dimensional microstructure in governing fast-charging behaviour and emphasise the need for spatially resolved design principles to develop safer, longer-lasting, and high-power batteries for sustainable energy applications.

Introduction

Power and energy densities are key parameters to develop better energy storage systems.¹ Unfortunately, in conventional Li-ion batteries (LiBs), these properties are antagonists, which

prevent long-range/fast charging in electric vehicles, as an example. Strategies need to be developed to address this issue or at least understand the limitation. Currently, electrode engineering is at the core of LiBs research to at least buffer this issue. Classical procedures involve optimising the loading (control of electrode thickness and “travelling” distance of the charges), electronic percolation (improving power density), and porosity (both ionic and electronic percolation) of electrodes to find an optimal ratio between energy and power for a given application. Unfortunately, the graphite negative electrode is the most affected by this limitation, even with

^aUniv. Grenoble Alpes, Univ. Savoie Mont Blanc, CNRS, Grenoble INP, LEPMI, Grenoble, France. E-mail: fannie.alloin@grenoble-inp.fr, claire.villevieille@grenoble-inp.fr

^bESRF, Experimental and Research Division, Grenoble, France

^cUniversité Grenoble Alpes, CEA, CNRS, IRIG, SYMMES, Grenoble, France



dedicated engineering. The underlying challenge is then to find the causes of this limitation and address these weaknesses.

To identify the process(es) that limit the power capability of the graphite electrodes, researchers investigated the impact of electrode engineering, in particular, the electrode porosity, as it allows tuning of electronic and ionic transport. Generally, the optimal porosity is set between 30% and 50%.^{2,3} Antartis *et al.* concluded that the optimal porosity of the electrode is around 45%, when graphite particle size is below 20 μm .⁴ Indeed, they did not observe any gain in specific capacity for porosities greater than 50%, since a similar and optimal wetting of the electrode was obtained above this value. However, in this case, the specific capacity fading was more pronounced and was related to a lack of mechanical strength at the electrode level, leading to progressive active material inactivity. For porosities smaller than 30%, the compactness of the electrode induces more stress on the particles during the lithiation process due to the swelling of the particles themselves (around 13% expansion of the unit cell volume⁵) and it induces specific capacity loss along cycling. For porosities between 30 and 50%, the authors attributed the lower specific capacity obtained at a C/5 rate (porosity of 37%) compared to the one obtained at C/20 to a limited transport of lithium ions through the denser graphite microstructure, while this limitation was less pronounced at a porosity of 49%. Similar results were obtained on LiFePO_4 electrodes, as demonstrated by Fongy *et al.* An electronic limitation is observed in the case of low electrode compacity (high porosity), whereas an ionic one occurs for denser electrodes.^{6,7}

A power limitation in an electrode could lead to lithiation heterogeneities in the electrode volume that could originate from ionic and/or electronic transport. Newman *et al.*, employing a modelling approach, accounted for such heterogeneities in porous electrodes by introducing a penetration depth concept.⁸ The concept of penetration depth, expressed in a dimensionless form, was later extended to incorporate other relevant parameters, such as salt concentration and transfer number. Based on the work of Doyle *et al.*,⁹ Fuller *et al.* modelled the discharge behaviour of a graphite/ MnO_2 cell and highlighted that the main process that limited power capability was the concentration gradient due to salt depletion.¹⁰ More recently, Gallagher *et al.* further developed the model and discussed the effect of current density on penetration depth in $\text{LiNi}_{0.8}\text{Co}_{0.15}\text{Al}_{0.05}\text{O}_2$ /graphite cells.¹¹ Tambio *et al.* using Gallagher's results demonstrated the importance of micrometric pore percolation in the homogenisation of salt concentration in the $\text{LiNi}_{0.5}\text{Mn}_{0.3}\text{Co}_{0.2}\text{O}_2$ electrode.¹² In all cases, the concept of penetration depth discusses the appearance of a salt concentration gradient along the electrode thickness that, in the worst case, could reach a concentration of zero. Dufour *et al.* investigated lithium concentration gradients as a function of electrode loading and C-rate with simulations.¹³ Using a spatial quantification of heterogeneity with the Normalised Absolute Average Deviation (NAAD) function, first introduced by Gu,¹⁴ heterogeneities in the composite electrode were observed in correlation with the formation of the

intercalation stages IV, II and I, stages mainly driven by a biphasic mechanism of lithium storage. Inversely, smaller heterogeneities were observed for solid solution phase mechanisms.

Experimentally, these inhomogeneities were also investigated. Lithium inventory mapping of electrodes (LIME) was developed combining both X-ray diffraction (XRD) and X-ray fluorescence (XRF) to probe at the same time the structural state of charge and the electrolyte concentration.¹⁵ Using imaging, *operando* optical microscopy experiments were performed.¹⁶ Kang *et al.* observed a front of lithiation from the separator/electrode interface toward the electrode/current collector interface, demonstrating a power limitation coming from the electrolyte.¹⁷ Unfortunately, quantitative estimation of the active material state of charge was not possible with this approach. X-ray diffraction, despite being a bulk technique with no visual evolution of the lithium concentration gradient, could play a key role. Based on energy-dispersive XRD, Yao *et al.* quantified lithiation gradients in a graphite electrode in a full cell graphite/NMC532. They observed that lithiation occurs first near the separator before propagating toward the current collector, demonstrating a limitation from the diffusion of lithium ions through the electrolyte.¹⁸ Tardif *et al.* used several literature data to report an average q scattering vector for the region containing LiC_6 (001) and graphite (002) Bragg reflections in correlation with the state of charge of a graphite half-cell, establishing a pseudo-calibration curve to determine the graphite state of charge from a diffraction pattern.¹⁹ The authors denoted a delithiation gradient from the separator toward the current collector and quantitatively estimated the heterogeneity in graphite delithiation with the NAAD function. Compared to the study by Dufour *et al.*, a similar evolution in the state of charge dispersion was observed for $x < 0.5$, but no dispersion was indicated for stage I formation ($x > 0.5$), which is inconsistent with the model results.

To date, there has been a lack of correlation between the lithiation heterogeneities in the electrode thickness and the electrode engineering parameters, in particular, the microstructure (porosity and tortuosity), but also with other engineering parameters such as the salt concentration. In this study, the microstructure of a graphite electrode with two porosities was investigated by means of tomography measurement and correlated to rate capability measurement and *operando* XRD using vertical profiling along the electrode thickness. The correlation between the electrochemical data and the structural properties evidenced the effect of the electrode's microstructure, in particular, in hindering Li-ion transport properties, which as a consequence, contributed to poor power capability of graphite electrodes.

Materials and methods

Electrode preparation and coin cell assembly

A suspension mixture composed of 80%_{wt} of SFG 6L graphite powder (Imerys), 10%_{wt} of Super C65 black carbon (Imerys)



and 10%_{wt} of PVDF HSV900 (Arkema) in *N*-methyl-2-pyrrolidone (NMP, Sigma Aldrich) was prepared and spread onto a copper foil which was used as a current collector of 10 μm thickness, using a doctor blade with a 600 μm blade height. The slurry was dried at 70 °C overnight, and electrode disks of 12 mm diameter were cut. From this process, porosities of 70 ± 5% (~120 μm of thickness) and a loading of 6 ± 0.5 mg cm⁻² were obtained. The reduction to 50% (75–80 μm) or 30% (50–55 μm) porosity was achieved using a calendering machine (MTI, MSK-HRP-01). The calendering process was performed at room temperature by applying a dedicated pressure, and then the electrodes were compressed at least three times at each pressure with a speed set to a value (7 on the apparatus). To remove the residual water, electrodes were dried overnight in a Büchi system at 90 °C under dynamic vacuum (10⁻³ bar), before being introduced into an Ar-filled glovebox. The electrodes were assembled on CR2032 coin cells in an Ar-filled glovebox with <1 ppm O₂ and H₂O. Half cells were mounted incorporating the graphite electrode, a glass fibre separator (Whatman) filled with 150 μL of LP30 (1 M LiPF₆ in EC/DMC 1:1%, Solvionic) and a 750 μm thick lithium metal disk of 12 mm diameter as a counter electrode (S4R supplier). Each electrochemical cycling was reproduced with three cells to ensure the reliability of the measurement. A standard deviation was extracted on the specific capacity obtained as a function of the cycling rate. This standard deviation is included in the plots analyzing the rate capability.

Cycling conditions and rate capability tests

All half cells were preliminarily cycled in a thermoregulated chamber at 25 °C (±0.1 °C), with two cycles at a C/20 cycling rate between 1.2–0.01 V vs. Li⁺/Li, with the first two cycles enabling proper formation of the solid electrolyte interphase (SEI). Then, the rate capability tests involve increasing the C-rate from C/10 to 4C, with each cycling at a specific rate being repeated three times. The cycling protocol uses a classical constant current-constant voltage (CCCV) procedure with a 30 min CV period between 1.2 and 0.01 V vs. Li⁺/Li. In the rest of the article, all potentials always refer to the redox couple Li⁺/Li.

Tortuosity measurement

Symmetric cells made of graphite electrodes were mounted in coin cells (12 mm diameter) and a glass fibre separator filled with 100 μL of 0.35 M LiPF₆ in EC/DMC (1:1%). The graphite electrodes used were the same (SFG 6L) as for rate capability tests, and the porosity ranged from 70% (pristine) to 50% and 30% by calendering. The coin cells were characterised by electrochemical impedance spectroscopy (EIS) at an open circuit voltage (OCV) between 1 MHz and 1 Hz with a perturbation amplitude of 10 mV using an SP150 (Biologic) at 25 °C (±0.1 °C). The impedance diagrams were recorded ten times every 30 minutes and the results were averaged. The measured impedance diagrams were fitted using a transmission line model (TLM) using Relaxis software as described by

Landesfeind *et al.*²⁰ (Note 1, SI). The ionic conductivity of the electrolyte was assessed using a dedicated conductivity cell.

X-ray holotomography measurements and data treatment

Graphite electrode disks of 50% and 30% porosity were cut in thin lamella (a few hundred micrometres in width) using a razor blade. The lamellas were glued to brass pins and placed in a sample holder made of PFA sealed under Ar using a UV-curing glue. Acquisitions were performed at the ESRF ID16B beamline²¹ using the X-ray holo-tomography technique.²² Scans composed of 4 consecutive acquisitions at each distance constituted 2505 projections, as well as 20 and 21 reference and dark images, respectively, that were recorded on a PCO edge 5.5 CMOS camera (2048 × 2048 pixels²) with a 17 μm thick LSO scintillator along a 360° rotation. For the incident X-ray beam, an energy of 29.45 keV and photon flux 3.4 × 10¹¹ ph s⁻¹ were measured, hence an exposure time of 10 ms per projection. Acquisitions were performed at a voxel size of 50 nm, resulting in fields of view of 102 × 102 μm². 3D reconstructions were achieved in two steps: (i) phase retrieval calculation using an in-house developed octave script based on a Paganin-like approach using a delta/beta ratio of 2740, and (ii) filtered back-projection reconstruction using ESRF software PyHST2.²³ Final volumes of 102 × 102 × 102 μm³ with a voxel size of 50 nm in a 32-bit floating point were obtained. Post-processing ring removal and 8-bit conversion were performed using a dedicated Matlab script.²⁴ Analyses were performed on the reconstructed 8-bit volumes using the ImageJ software.²⁵ The different phases were segmented using a machine learning based random forest classifier embedded within the Ilastik software.²⁶ Additional details on image analysis and tortuosity calculation are presented in Note 2, SI.

X-ray diffraction measurements and data treatment

X-ray diffraction experiments were performed at the ESRF ID31 beamline. Coin cells were cycled at C/4, C/2 and C/1 rates using an SP150 potentiostat (Biologic) in a thermoregulated environment at 25 °C (±0.1 °C). To ensure a reliable vertical profiling experiment, the coin cells were aligned parallel to the beam so that the X-rays travelled through the whole diameter of the graphite electrodes. For the electrode with 50% porosity, the electrode thickness (around 75 μm) was probed with steps of 16 μm over a thickness of 90 μm. In the end, five *z*-positions localised in the electrode thickness were analysed, and each of them was found to be in agreement with their relative position in the electrode thickness *L* (0.1 *L*, 0.3 *L*, 0.5 *L*, 0.7 *L* and 0.9 *L*; 0.1 *L* being near the separator and 0.9 *L* near the current collector). For the electrode with 30% porosity, the electrode thickness (around 50 μm) was probed with steps of 5 μm. Nine *z*-positions were analysed corresponding to relative positions from 0.1 *L* to 0.9 *L*, with steps of 0.1 *L*.

A Pilatus 2 M CdTe 2D detector (Dectris) was used for the acquisition of the diffracted signal, positioned roughly 1 m from the sample. The beam energy was set at 75 keV, and the beam was focused on the sample (approximately 5 μm ×



15 μm , vertical \times horizontal). The 2D images were integrated into the 1D diffraction pattern using the pyFAI package.²⁷

Data treatment was performed using Python software with *Matplotlib*²⁸ and *LMFIT*²⁹ libraries. A baseline subtraction on the 1D diffraction patterns was realised using a SNIP (statistics-sensitive non-linear iterative peak-clipping) algorithm from the PyBaseline library.³⁰

Results and discussion

Electrochemical characterisation

To assess power limitations, we investigated graphite electrodes with two different porosities, 50% and 30%, as a function of the applied cycling rate (rate capability tests^{31–33}) and of the salt concentration in the electrolyte (1 M, 0.7 M and 0.35 M LiPF_6 in EC/DMC 1:1 v_v). Fig. 1a shows the evolution of the galvanostatic fraction (CC) over the total specific capacity obtained by CCCV depending on the applied C-rate for 50% and 30% porosity graphite electrodes. The inset shows the specific galvanostatic capacities obtained for each cycle for both electrode porosities. At slow cycling rates (C/20–C/6), stable specific galvanostatic capacities were obtained (slightly decreasing from 383 mAh g^{-1} to 358 mAh g^{-1}) for both electrode porosities. It should be noted that the obtained specific capacities exceed the theoretical specific capacity of graphite because of additional charges coming from the adsorption of Li^+ on nanoparticles of carbon additive, increasing the maximal specific capacity of the composite electrodes. A difference appears at the C/4 rate, when a lower specific galvanostatic capacity is observed for the electrode with 30% porosity, compared to the one at 50% porosity. Notably, at fast charging rates (above C/2), the electrode can no longer reach graphite's theoretical specific charge. By increasing the cycling rate to

2C, a larger difference is noticed in the achievable capacity, as a function of the electrode porosity. The highest difference is obtained at C/1.5, with a galvanostatic specific capacity of 230 mAh g^{-1} for the electrode with 30% porosity, whereas 273 mAh g^{-1} is achieved for the electrode with 50% porosity. For higher cycling rates (2C–4C), a stabilisation of the specific galvanostatic capacities is observed, representing less than 20% of the total specific capacities for both porosities. At this stage, Li plating could also play a role but from an electrochemical perspective, monitoring lithium plating during lithiation remains challenging, while it becomes less during delithiation as lithium is oxidized. Careful examination of our delithiation curves revealed no evidence of a plateau associated with Li plating, even at high charging rates. However, in this range and even at a faster charging rate, we suspect that the lithium counter electrode takes the lead in terms of kinetic limitation, inducing a large counter electrode polarization. Lu *et al.* further investigated the failure mechanisms for fast charged Li metal batteries with liquid electrolyte.³⁴ They demonstrated that at rates higher than the 1C rate, already Li can be detrimental for cycling. In addition to the Li metal counter electrode limitation, the half-cell could deliver many “capacitive” charges since no capacity from intercalation could be achievable. This explains why the specific galvanostatic capacity reaches a plateau for high C-rates.

To further characterise the electrochemical behaviour of the two electrode porosities, the lithiation profiles obtained at C/4 are compared (Fig. 1b). Regarding the two last potential plateaus (attributed to stage II and stage I formation,^{35,36} around 0.8 and 0.05 V), a similar starting potential can be seen; however, the plateau of the potential shows a higher tilt for the electrode with 30% porosity. This is even more visible in Fig. 1c, where the peaks obtained by differential capacity analysis (DCA) are broader and reach lower intensities for the elec-

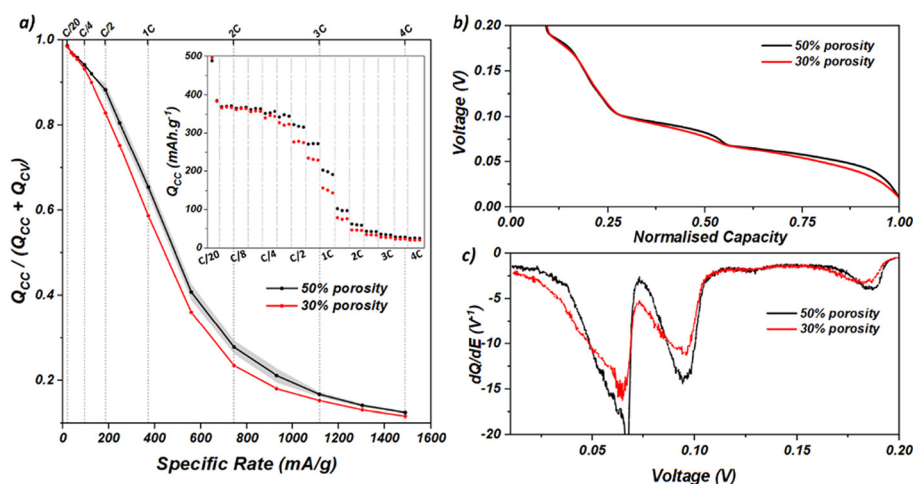


Fig. 1 Rate capability test performed on graphite electrodes with 50% and 30% porosity (black and red curves, respectively) cycled vs. Li in half cell configuration with the LP30 electrolyte. (a) Proportion of galvanostatic charge (CC) over the total specific capacity obtained by CCCV with a CV period of 30 min, as a function of the C-rate applied. The inset shows the specific galvanostatic capacities obtained during the rate capability tests. (b) Lithiation profiles obtained at the C/4 rate for each electrode porosity. (c) Differential Capacity Analysis (DCA) of the lithiation profiles obtained at the C/4 rate.



trode with 30% porosity. All these features highlight higher limitations in the graphite electrode lithiation for 30% porosity, probably linked to electronic and/or ionic transport.

To verify whether the limitation is caused by electronic or ionic percolation, similar rate capability tests were carried out on graphite half cells by changing the salt concentration from 1 M to 0.7 M and 0.35 M LiPF_6 in EC/DMC 1:1%_v. For all the electrolytes, the first formation cycle was performed at C/20 to ensure a good SEI formation. As it is well known that the SEI properties are also dependent on the electrolyte and salt concentration,^{37–39} we compared the first lithiation and it is provided in the SI (Note 3). The potential of the formation of the SEI remains the same *i.e.* 0.8 V despite having a different salt concentration, as well as the “length” of the plateau indicating that the Coulomb exchanges are rather similar. It indicates that the SEI properties remain similar in the three cases, even if we cannot exclude a small difference in the chemical properties. Fig. 2a shows the evolution of the galvanostatic contribution depending on the salt concentration as a function of the C-rate. The inset shows the specific galvanostatic capacities for all salt concentrations. Two features are observed: (i) the specific galvanostatic capacities are lowered by decreasing the salt concentration from the C/10 to the 2.5C rate and (ii) the decrease of galvanostatic contribution with the increase in the C-rate is faster when decreasing the salt concentration. Again, at a rate of 2.5C and above, the lithium metal counter electrode plays a key role independent from the salt concentration in the electrolyte. In Fig. 2b, one can notice that decreasing the salt concentration induces a less “marked” curve at C/4, losing the typical potential plateau shape of the

graphite staging process. From the DCA curves in Fig. 2c, two phenomena can be observed: (i) the three peaks are shifted toward lower potentials (shown by the horizontal black arrows) on decreasing the salt concentration; this is due to the higher overpotentials of lithiation originating from the lower concentrations (inducing higher ohmic drop) and/or the lower kinetic of lithiation; (ii) the peaks reach lower intensities (shown by the vertical black arrows) that highlights a partial loss of the flat potential features because of a more dispersed process in the electrode volume. The effect of salt concentration supports the hypothesis of an ionic limitation in the electrode. Decreasing the salt concentration causes higher depletions of lithium ions in some part of the electrode volume, inducing lower specific capacities for a given cycling rate and the loss of the typical potential plateau shape of graphite lithiation.

The rate capability tests coupled to the salt concentration decrease demonstrate that the ionic diffusion of lithium is the limiting factor regarding the power ability of graphite electrodes. These results are in agreement with the literature studies demonstrating similar ionic transport limitations in graphite electrodes. A decrease of the electrode porosity is known to increase the tortuosity, which is responsible for higher diffusion times of lithium ions through the electrode microstructure for a given distance. Tortuosity can be measured with two different methods, either by electrochemical impedance spectroscopy (EIS) and/or by X-ray tomography measurements or focused-ion beam scanning electron microscopy (FIB-SEM). The former is simply referred to tortuosity parameters, whereas the second one is generally called geometric tortuosity. The absolute values between them are different, but the

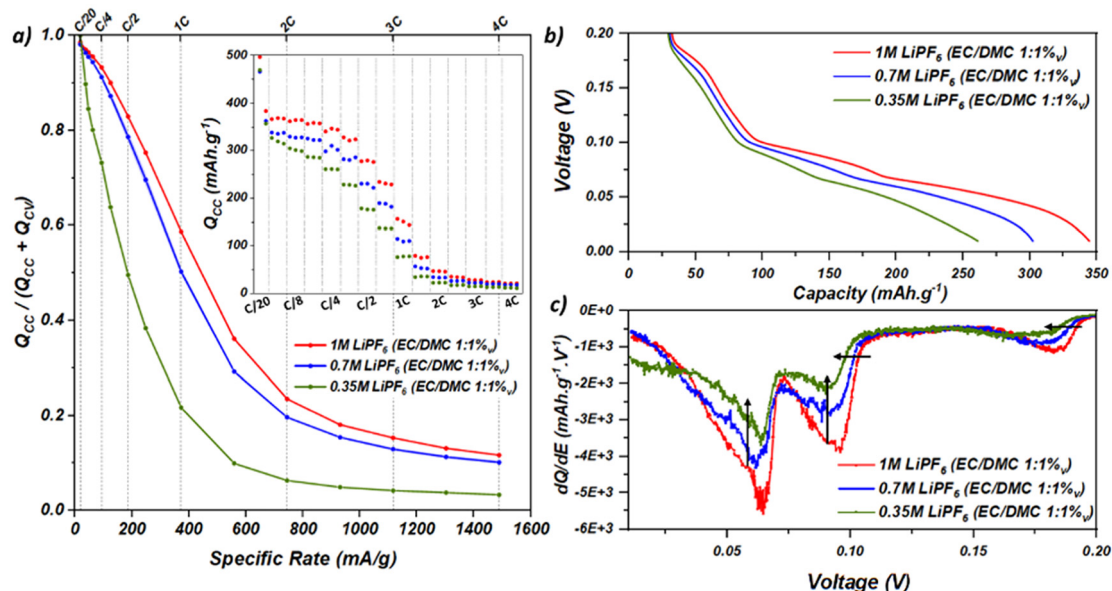


Fig. 2 Rate capability test of the graphite electrode (30% porosity) cyclized vs. Li^+ in half cells with 1 M, 0.7 M and 0.35 M LiPF_6 in EC/DMC 1:1%_v (red, blue and green curves respectively). (a) Proportion of the galvanostatic charge (CC) over the total specific capacity obtained by CCCV with a CV period of 30 min, as a function of the applied C-rate. The inset shows the galvanostatic capacities obtained during the rate capability tests. (b) Lithiation profiles obtained at the C/4 rate for each salt concentration. (c) Differential capacity analysis of the lithiation profiles obtained at the C/4 rate.



trend remains similar. Yet, we measured the ionic tortuosity using EIS (presented in Note 1, SI). For an electrode with 50% porosity, a tortuosity of 7 ± 0.2 was obtained while that of 9.4 ± 0.7 was obtained for an electrode with a porosity of 30%. The values obtained are in the upper range of the reported values for graphite electrodes with similar porosities and particle morphologies (from $\tau = 5$ to 10).^{20,40–43} Still, the ionic tortuosity difference between the two electrode porosities is significant, and it supports a longer diffusion of lithium ions through the electrode thickness for a porosity of 30%.

Morphological characterisation

The graphite electrodes with 50% and 30% porosity were also characterised by X-ray holotomography (ID16B, ESRF, Grenoble) to assess the microstructure of the electrodes (Fig. 3a and d). From the segmented tomographs (methodology is explained in Note 2, SI), each phase (graphite SFG 6L, carbon-binder domain (CBD), and porosity) was characterised in terms of volume fraction and median local thickness. Table 1 summarises the main results obtained from the X-ray holotomography measurement for each electrode. First, a good agreement can be found between the theoretical (estimated from the weight and density of the components) and experimental values when it comes to the volume fraction of the different phases, validating the segmentation process. Due to the reached resolution (voxel size of 50 nm), a small fraction of the pores (<100 nm) was possibly not accessible and instead

attributed to graphite and/or CBD phases, as observed in the slight underestimation of the porosity volume fraction. It seems that calendaring does not have a huge impact on the CBD domains since they are of similar thicknesses (195 vs. 240 nm), in the range of the experimental resolution. As expected, the pore size decreases when the porosity of the electrode is decreased (from 510 nm to 370 nm). From the porosity phase, the pore intra-connectivity was evaluated and shows proper wettability of the electrode (100% and 97% for 50% and 30% porosity, respectively). Still, calendaring slightly decreases the intra-connectivity, probably because of the closing of some pores. We also analysed the distribution of porosity along the electrode thickness for both porosities as presented in Note 4 (SI). We noticed that calendaring enabled a homogenisation of the porosity along the electrode thickness, whereas at 50% porosity a higher distribution was observed with larger porosity at the separator/electrode interface reaching 60%.

The geometric tortuosity was estimated through geodesic/Euclidean distances along the through- and in-plane directions (Fig. 3b and e). The in-plane and through-plane tortuosities are given in Fig. 3c and f for the two electrode porosities. A close in-plane tortuosity is found for both electrode porosities (1.13 vs. 1.33), whereas the through-plane tortuosity (from where the calendaring is effective) was increased by the calendaring step (1.4 vs. 2.0 for 50% and 30% porosity respectively). A thinner distribution is observed for the in-plane direction

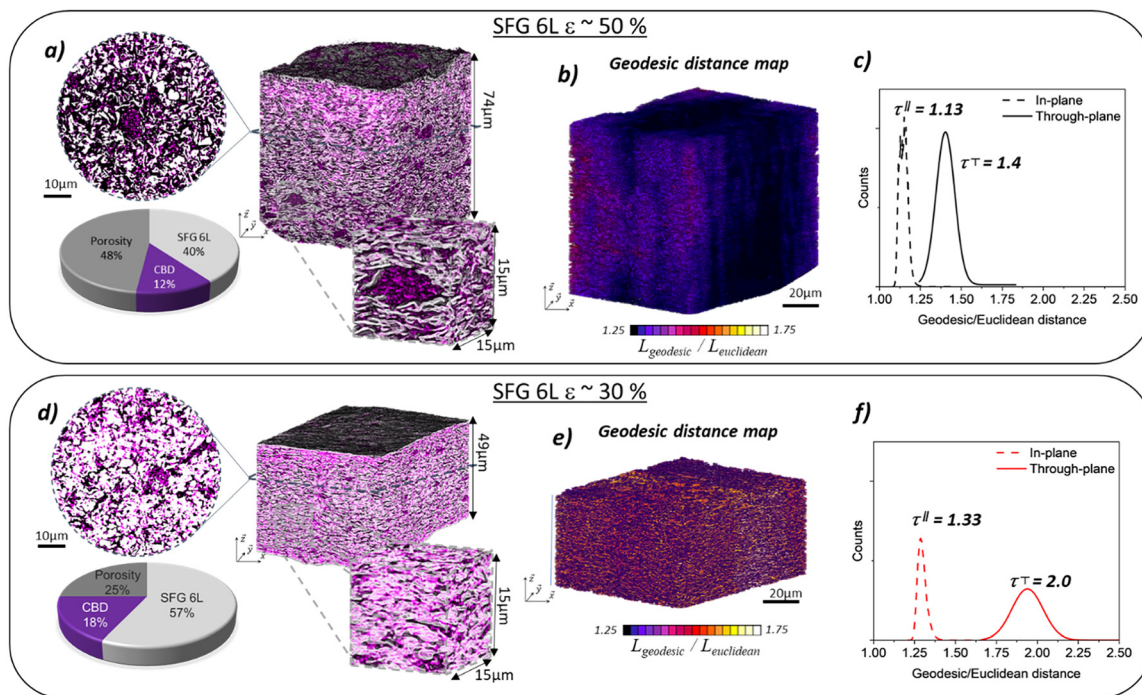


Fig. 3 X-ray holotomography results obtained at the ID16B beamline at ESRF. (a) Segmented image of the 50% porosity graphite electrode, with the volume fraction of each phase. (b) Geodesic distance map for the 50% porosity graphite electrode. (c) Cumulative geodesic/Euclidean distances for the 50% porosity graphite electrode. (d) Segmented image of the 30% porosity graphite electrode, with the volume fraction of each phase. (e) Geodesic distance map for the 30% porosity graphite electrode. (f) Cumulative geodesic/Euclidean distances for the 30% porosity graphite electrode.



Table 1 Results obtained from the segmentation of the X-ray holotomography experiments for 50% and 30% porosity graphite electrodes

Electrode	Graphite		CBD		Porosity		CBD median local thickness	Pores' median local thickness	Pores' intra-connectivity
	% V_{theo}	% V_{exp}	% V_{theo}	% V_{exp}	% V_{theo}	% V_{exp}			
50%	37%	40%	13%	12%	50%	48%	195 nm	510 nm	100%
30%	53%	57%	17%	18%	30%	25%	240 nm	370 nm	97%

compared to the through-plane direction. The geodesic distance maps for in-plane and through-plane directions are given in Note 5 (SI), with values in agreement with the literature.⁴⁴ These observations correlate with the flake shape of graphite particles that are naturally oriented with their basal plane parallel to the current collector plane, generating more tortuous pathways in the through-plane direction. The results are also in agreement with the tortuosity estimated *via* EIS, demonstrating the detrimental effect of decreasing the porosity from 50% to 30% by calendaring. The estimated values with both techniques are different because the measured tortuosity is not equivalent. Indeed, whereas electrochemically determined tortuosity is sensitive to all the interactions between lithium ions, the counter anion and the porous structure, the geometrical tortuosity does not account for it and is limited to geodesic distance evaluation restricted by the imaging resolution.⁴⁵

From these microstructures, diffusion simulations were performed using the software TauFactor by Cooper *et al.*⁴⁶ This software was developed to compute effective transport properties in 2D or 3D microstructures by setting specific boundary conditions. Here, the 3D volumes obtained by X-ray holotomography were injected and the effective diffusivity was computed for each electrode porosity. By convention, the methodology imposes the definition of salt concentration boundaries at the separator/electrode and electrode/collector interfaces that were set to $C_{\text{sep}} = 1$ and $C_{\text{cc}} = 0$, since it is commonly accepted that the concentration will be minimal at the current collector side. Then, by solving the Laplace equation for steady-state diffusion, the tortuosity factors were computed as described in Note 2 (SI). This methodology, even though it might seem peculiar, still allows a fair comparison between both electrodes. The simulation results are shown in Fig. 4, with 3D views of the concentration gradient for both porosities (Fig. 4a and b). Tortuosity factors of 4.65 for the electrode of 50% porosity and 17.9 for the electrode of 30% porosity were obtained. The distribution of salt concentration along the electrode thicknesses was also investigated and is shown in Fig. 4c. A linear decrease of the normalised concentration was observed by penetrating the electrode thickness for a porosity of 30%, whereas two slopes (visible with the dashed lines) were observed for the electrode of 50% porosity, with a slope break around 30 μm . This demonstrates a better homogeneity of the electrode's microstructure for a porosity of 30%, due to the higher calendaring pressure. Furthermore, the evolution of the median local pore size as a function of the electrode depth is displayed in Fig. 4d. The profile shows a gradient from a larger pore size towards the separator to smaller ones closer to

the current collector interface for the poorly-calendered electrode (50% porosity) with variation of more than 10% to the average median local pore thickness value ($d_{50} = 510$ nm). The same trend is already reported for the local porosity volume fraction as a function of depth in Note 4, SI (Fig. S4a). In contrast, a more homogeneous distribution along the electrode depth is reported for the calendered electrode (*i.e.* 30% porosity) (less than 3% variation to its average median local pore thickness value of 370 nm). Moreover, the dual-slope behavior observed for the 50% porosity electrode shows an inflexion point that corresponds to the moment when median local pore size goes below the average value of the entire microstructure (at a depth of 33 μm). These observations support the hypothesis of a more homogenous salt concentration in the more calendered microstructure.

Structural characterisation

From the preliminary observations obtained by electrochemical and morphological investigations, we expect heterogeneities of lithiation along the electrode thickness that should be more pronounced for a porosity of 30%. Using the methodology established in this first paper,⁴⁷ these inhomogeneities were assessed by z-profiling experiments using X-ray diffraction at ID31 (ESRF, Grenoble) on the two electrode porosities cycled in the half cell *vs.* the Li metal with the LP30 electrolyte at 25 °C. For the sake of clarity, the lag time required for one full z-scan is ~ 0.018 h (example of the electrode with 30% porosity) which represents a delta of 0.5% SoC at C/4, 1% SoC at C/2 and 2% SoC at 1C between the position close to the separator and the one close to the current collector; thus it cannot explain the behavior discussed below. In the following section, we will discuss the structural state of charge of graphite determined by XRD, assigned to x in Li_xC_6 . This structural state of charge should be differentiated from the electrochemical state of charge of the cell (SoC_{cell}), which corresponds to the accumulated amount of charges.

Structural state of charge determination. Fig. 5 summarises the experiment realised on the lithiation of the graphite half-cells, with the experimental set-up (Fig. 5a), the X-ray diffractograms obtained during the *operando* measurement at the C/4 rate for the porosity of 50%, as an example (Fig. 5b), and the electrochemical signature obtained at C/4, C/2 and C/1 rates for both porosities (Fig. 5c). From the diffraction patterns obtained in Fig. 5b, it was possible to extract the structural state of charge of graphite (x in Li_xC_6) using the methodology developed in this article and the model curve obtained from quasi thermodynamic equilibrium.⁴⁷ A summary of the methodology is described in Note 6 (SI) and the protocol of the



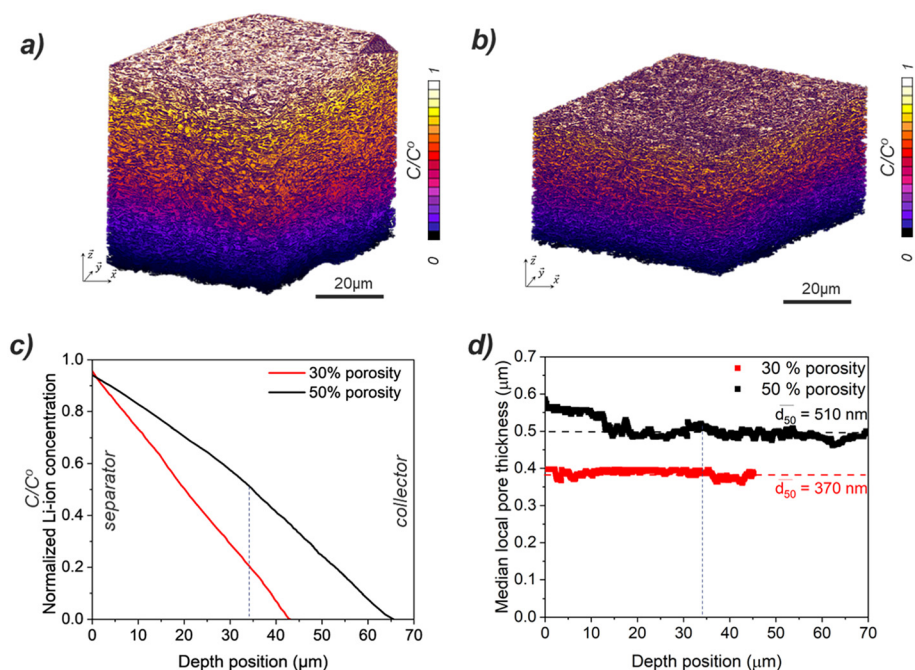


Fig. 4 3D views of the concentration gradient in the electrolyte estimated from the electrode microstructure of (a) 50% porosity and (b) 30% porosity. (c) Normalized concentration profiles along the electrode thicknesses and (d) evolution of the median local pore thickness along the electrode depth for both electrodes.

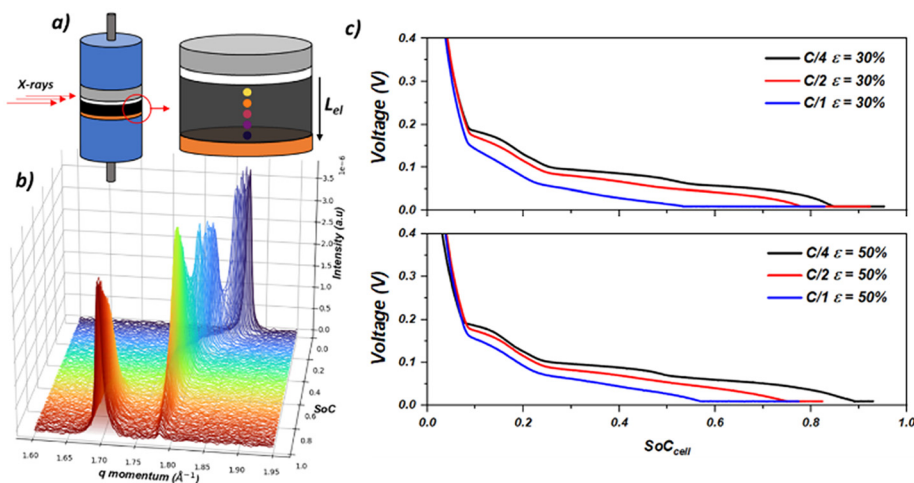


Fig. 5 Experimental set-up used at ID31 beamline (ESRF), and the main results obtained. (a) Scheme of the Swagelok® cell probed by X-rays along the thickness of the electrode. (b) 3D waterfall plot of the diffraction patterns obtained upon lithiation of the 50% porosity electrode at the C/4 rate, for the position near the separator (0.1 L). (c) Evolution of the cell voltage as a function of SoC_{cell} for the two electrode porosities, obtained at C/4, C/2 and C/1 rates.

z-profiling experiment is given in the Materials and methods section. The electrochemical signatures of the two cells at the C/4 rate are displayed in Fig. 6a and b, for the 50% and 30% porosities, respectively. The corresponding Fig. 6c and d show the evolution of the structural state of charge (x in Li_xC_6) for each position in the electrode thickness (from 0.1 L, that is close to the separator, to 0.9 L, close to the current collector) depending on the electrochemical state of charge of the cell

(SoC_{cell} , determined from the integration of current passing through the cell with time). The dispersions of x in Li_xC_6 appear during the potential plateaus for both porosities, with a lithiation front directed from the separator toward the current collector side. This observation leads us to conclude that the limiting process in the power capability of these graphite electrodes is the diffusion of lithium ions through the electrode thickness, since the lithiation front would go in the



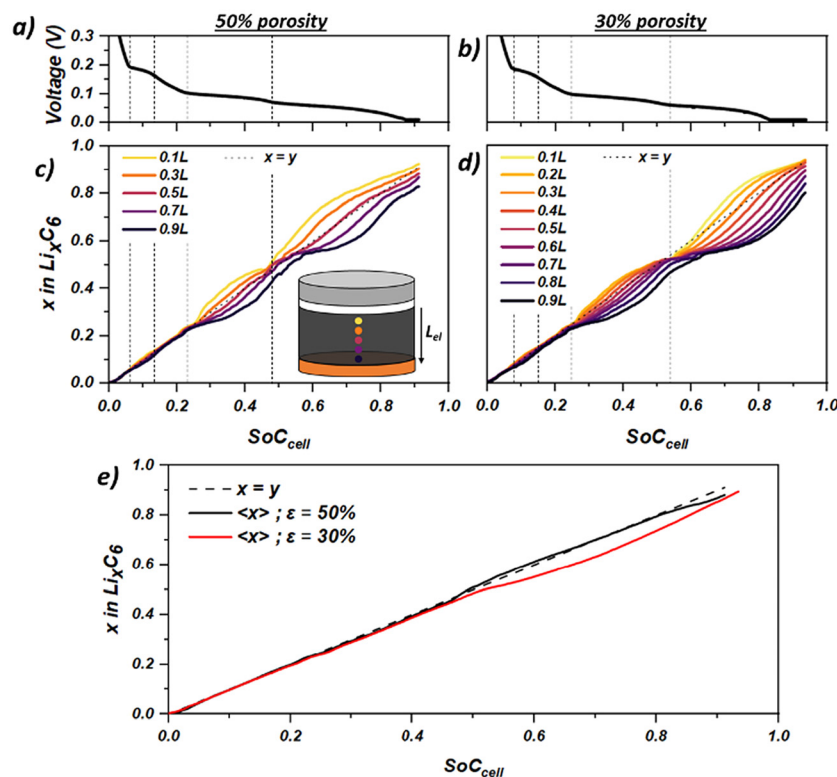


Fig. 6 Evolution of the structural state of charge (x in Li_xC_6) for both porosities upon lithiation at the $C/4$ rate. (a) and (b) Graphite potential evolution as a function of SoC_{cell} , respectively, for 50% and 30% porosity electrodes. (c) and (d) Structural state of charge (x in Li_xC_6) evolution as a function of SoC_{cell} , respectively, for 50% and 30% porosity electrodes. (e) Mean structural state of charge ($\langle x \rangle$) for both porosities as a function of SoC_{cell} .

opposite way in the case of an electronic limitation. Furthermore, graphite possesses good electronic conductivity and calendaring the electrodes helps to gain electronic percolation, particularly with the usage of a conductive agent. However, at a very fast charging rate, we cannot exclude that a mixed-control regime could take over.

Assuming that each electron injected into the graphite conduction band induces the insertion of one lithium ion, a perfect match between the structural state of charge (x in Li_xC_6) and the electrochemical one (SoC_{cell}) should be observed. We compared the evolution of the mean x ($\langle x \rangle$) along the electrode thickness with the $x = y$ straight line in Fig. 6e. One can observe a very good match between the $x = y$ line and the mean x in Li_xC_6 for the electrode with 50% porosity, even if a slight deviation is noticed around 0.85 SoC_{cell} which correlates with the holding potential period (CV). For the electrode with 30% porosity, a good match is observed from 0 to 0.5 SoC_{cell} ; above this value, a deviation reaching a maximum of 7% appears with the structural state of charge evolving slower than the electrochemical one. To prove that this feature was not generated by the data treatment and is reliable, another method of x in Li_xC_6 determination was applied using the proportions of stage II and stage I phases (see Note 7, SI). A good agreement is obtained between the two methods.

We list several hypotheses to explain the deviation observed for the electrode with 30% porosity:

Upon cycling, graphite particles undergo volumetric changes reaching +10% at the end of lithiation,⁵ translated into a unidirectional expansion increasing the electrode thickness. As a consequence, the z -positions that were probed by the X-ray beam at the beginning of the lithiation are not exactly the same as at the end. Since the electrode thickness expansion is unidirectional and oriented toward the separator, we suppose that the z -positions probed near the current collector do not significantly change upon lithiation, but near the separator the initially probed graphite particles are no longer in the field of the probe as schematised in Fig. 7. With a rough calculation for the electrode porosity of 30%, we estimated that the 0.1 L position initially localised at 5 μm near the separator should be localised at 12 μm from the separator in the end of lithiation (~ 0.2 L). Therefore, the volume probed at the end of lithiation might be slightly less representative of the mean structural state of charge (x in Li_xC_6), which is a possible explanation for the deviation observed. To justify the difference between the two electrode porosities, we suspect that a large porosity (50%) is more likely to buffer the electrode thickness expansion. Indeed, with a larger fraction of pores, a higher volume is available to accommodate the volume changes, reducing the total thickness expansion upon



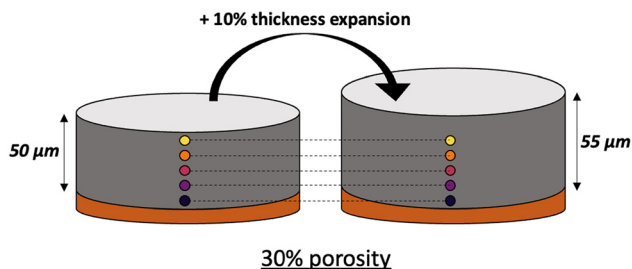


Fig. 7 Scheme showing the 30% porosity graphite electrode expansion upon lithiation. The coloured points represent the z -positions probed by the X-ray beam, before and after cycling to show the impact of uniaxial volume changes.

lithiation. Additionally, the dispersion in the structural state of charge (x in Li_xC_6) being less important for 50% porosity, this effect is again reduced. To verify this point, we carried out an additional experiment using a nano-dilatometer measurement and compared a commercial graphite electrode (around 30% porosity) and a home-made electrode (around 70% porosity). As explained in the SI (Note 8), it is difficult to establish a direct correlation between the electrode volume expansion and graphite particle expansion, since microstructural components such as the binder and porosity play significant roles in accommodating volumetric changes. As can be seen in Fig. S11, nano-dilatometric measurements were conducted on a graphite electrode with 70% porosity across several cycles at a very low cycling rate (C/40, imposed by the ceramic T-frit separator). The theoretical delithiation of graphite particles (represented by the dotted line) was compared to the measured dilation obtained from the dilatometer. The observed agreement between the dilation profiles was achieved by applying a factor of 0.25 to the theoretical particle dilatation rate, indicating that only one quarter of the particle-level expansion is reflected at the electrode level. This implies that approximately 75% of the particle's expansion is accommodated by electrode porosity and binder deformation. A similar experiment using a commercial electrode demonstrated that when the graphite porosity decreases to 30%, the electrode is capable of buffering only 50% of the volume change.⁴⁸

Another hypothesis relies on the consumption of charges by parasitic reactions such as SEI and/or adsorption. As an example, we suppose that upon lithiation, because of the volume expansion, new “fresh” surfaces of graphite particles are exposed to the electrolyte and solvent reduction can proceed. This would imply the consumption of charges without modifying the structural state of charge, which can contribute to the slight deviation observed. However, we do not expect a large amount of charges to be consumed by this SEI formation. This solely cannot explain the observed deviation.

Heterogeneities of lithiation. To quantify the heterogeneity of lithiation along the electrode thickness, an absolute average deviation (AAD, eqn (1)) was calculated by analogy with the NAAD.^{13,19}

$$\text{AAD}(x) = \frac{1}{L} \int_{z=0}^{z=L} |x(z) - x_z| dz \quad (1)$$

where L is the electrode thickness, $x(z)$ is the structural state of charge at the corresponding z -position and x_z is the mean structural state of charge along the electrode thickness. It should be noted that the NAAD parameter has a sensitivity depending on the region of x in Li_xC_6 , with a higher sensitivity near $x = 0$. In contrast, the AAD parameter expresses the absolute deviation in x in Li_xC_6 with the same sensitivity on the overall lithiation range, bringing the possibility to compare its evolution from $x = 0$ –1 quantitatively.

Fig. 8b shows the plot of the evolution of the AAD parameter depending on the SoC_{cell} for the graphite electrode of 50% porosity cycled at the C/4 rate. Data were correlated with the graphite electrode potential and are shown in Fig. 8a and, on the right y -axis, with the evolution of $d(\text{SoC})/d(E) = f(\text{SoC}_{\text{cell}})$ (this representation is analogous to the DCA analysis but expressed as a function of the SoC_{cell}). One can observe that low values of AAD are obtained for the regions 1 and 3, involving the transitions of graphite to LiC_{72} (stage I') and LiC_{36} to LiC_{24} (stage IV \rightarrow stage III), transitions driven by solid solution mechanisms. In contrast, a bell-shaped curve is observed for the AAD parameter in correlation with the peaks observed on the d_{SoC}/d_E representation; it should be noted that each peak is linked to a potential plateau ascribed to biphasic mechanisms.

The origin of the bell-shaped curve is linked to the nature of the lithiation mechanism, and here we can take the example of region 2 associated with the stage I' to stage IV transition as described in Fig. 9:

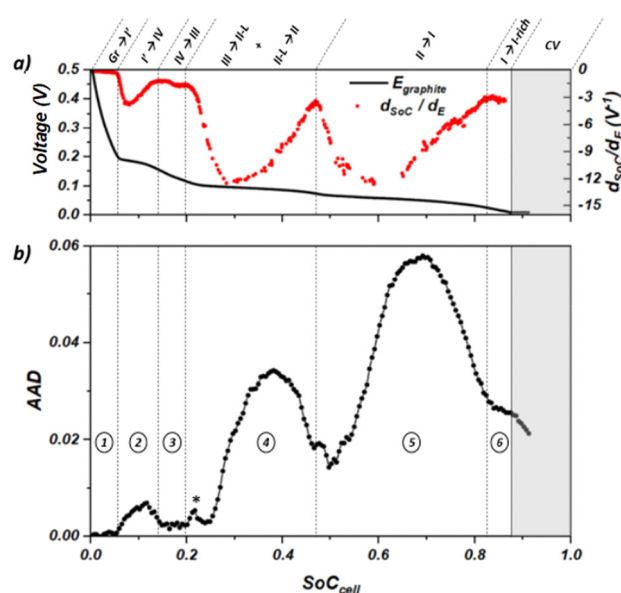


Fig. 8 Correlation between the AAD parameter and the electrochemical signature obtained at the C/4 rate for the graphite electrode with 50% porosity. (a) Evolution of the graphite potential on the left axis and d_{SoC}/d_E on the right axis, as a function of SoC_{cell} . (b) Evolution of the AAD parameter as a function of SoC_{cell} .



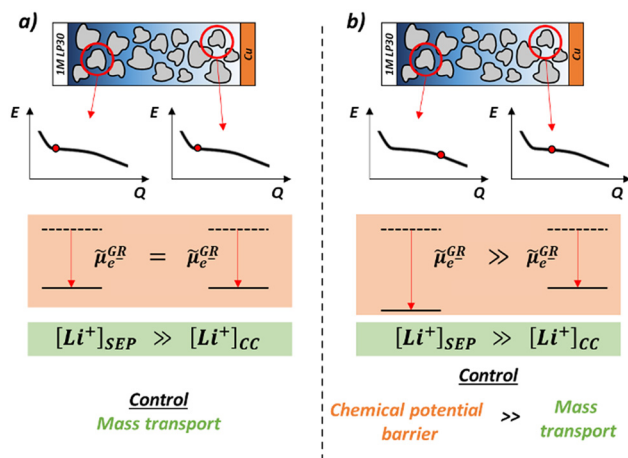


Fig. 9 Scheme explaining the AAD bell-shaped evolution. (a) Graphite particles display similar electrochemical potentials ($\tilde{\mu}_e^{GR}$), meaning that the lithiation is favoured near the separator. (b) A chemical potential barrier limits the lithiation near the separator and the lithiation becomes favourable near the current collector. $[Li^+]_{SEP}$ and $[Li^+]_{CC}$ correspond to the lithium concentration in the electrode porosity near the separator or near the current collector.

(i) When the graphite electrode reaches stage I' (LiC_{72} stoichiometry, Fig. 9a), no heterogeneity is observed, meaning that graphite enters the first potential plateau of lithiation homogeneously in the electrode volume. Since this transition (stage I' to stage IV) is mainly driven by a biphasic mechanism, the electrochemical potential associated with lithium intercalation is rather constant and homogeneous along the electrode thickness. Then, the consumption rate of lithium ions is controlled only by the local concentration of salt in the electrolyte, which becomes more and more heterogeneous along the electrode thickness upon charging due to the tortuous microstructure. This is responsible for the generation of a salt concentration gradient with depletions in the current collector direction; the consequence is the appearance of heterogeneities of the state of charge (increase of the AAD parameter, increasing part of the bell-shaped) with favoured lithiation at the separator/electrode interface.

(ii) This biphasic transition ends earlier for graphite particles near the separator side, implying that their electrochemical potential begins to change by entering the solid solution domain (Fig. 9b). The latter acts as an activation barrier and limits the intercalation of lithium ions. In these conditions, the rate of lithium ion consumption is not only controlled by the salt concentration but also by the electrochemical potential that increases the cost for lithium intercalation. It results in a favourable lithiation of the graphite particles that are still in the biphasic transition, *i.e.* near the current collector side, and a homogenisation of the structural state of charge (x in Li_xC_6) is observed (decrease of the AAD parameter leading to the decreasing part of the bell-shaped curve).

Pursuing our investigation with region 4, one can notice a slight increase of dispersion in x between 0.2 and 0.25 SoC_{cell} ,

shown by an asterisk in Fig. 8b, which can be due to the transition between stage III and stage II-L (LiC_{24} to LiC_{18}) that is partially driven by the biphasic mechanism as discussed in a previous report.⁴⁷ Entering the stage II formation at 0.25 SoC_{cell} , a large increase in the dispersion of x (second largest bell-shaped curve) is observed. The larger heterogeneity compared to the first bell-shaped curve (stage IV formation) is related to the higher number of exchanged coulombs on this second potential plateau. At the end of stage II formation, the dispersion in x did not disappear totally, indicating that the re-homogenisation of the state of charge was partial, despite the potential drop between the two last potential plateaus. Therefore, the dispersion in x observed in region 5 during the biphasic transition between stage II to stage I (LiC_{12} to $\sim Li_{0.9}C_6$) is even more pronounced. Between 0.83 and 0.88 SoC_{cell} (region 6), a rather stable AAD evolution is noticed and correlates with the transition between stage I and the enriched-stage I, materialised by the stable period on the d_{SoC}/d_E representation. This specific feature is like the trend observed for the transitions involving solid solutions (Gr \rightarrow stage I' and stage IV \rightarrow stage III, regions 1 and 3 respectively); it supports the existence of solid solutions during the enrichment of stage I to form the LiC_6 phase as discussed previously.⁴⁷

The impact of the porosity on the AAD parameter can be seen in Fig. 10a. A similar evolution of the AAD parameter of the two electrodes with different porosities is noticed until 0.25 SoC_{cell} , indicating that the distribution in x is similar in both cases and independent of the microstructure of the electrodes. In contrast, a larger heterogeneity in x is observed for the second bell-shaped curve (associated with stage II formation) for the electrode with a porosity of 30%. The latter is highlighted in Fig. 10b, where the structural state of charge at the current collector side (0.9 L) is plotted for both porosities. Starting from 0.25 SoC_{cell} , the 0.9 L position for 30% porosity is more delayed in terms of the structural state of charge evolution (below the $x = y$ line). This is directly linked to the so-called penetration depth of lithium ions, which is lower for this electrode porosity (higher tortuosity), indicating that the kinetics of lithiation at an equivalent relative depth (0.9 L) is lower. Pursuing the last bell-shaped curve, the dispersion in x is even larger for 30% porosity. It should be noted that at the end of the galvanostatic part (shown by a star on both AAD curves), the electrode with 30% porosity is way more heterogeneous in the structural state of charge along its thickness, demonstrating the limitation for power applications.

Cycling rate and current distribution. Here, we discuss the rate capability measurement of the 50% porosity graphite electrode in terms of dispersion in x (at C/4, C/2 and C/1, Fig. 11a). For very low SoC_{cell} , a similar AAD is observed which is consistent with a cell that is not limited by any transport phenomena. However, pursuing the lithiation, larger heterogeneities are observed by increasing the cycling rate, with higher AAD values at the maxima of the bell shapes. Additionally, in the regions where the structural state is re-homogenised (such as at $SoC_{cell} = 0.5$), one can notice the higher AAD values by



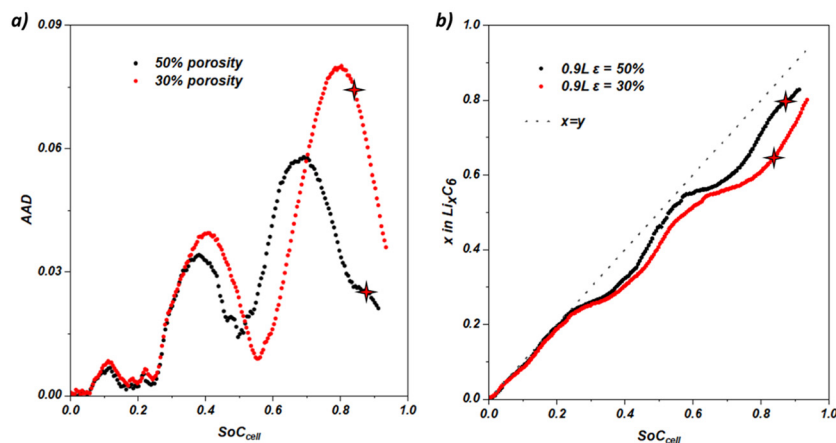


Fig. 10 Comparison of the lithiation heterogeneity for the 30% and 50% electrode porosity. (a) Evolution of the AAD parameter as a function of SoC_{cell} for both porosities. (b) Evolution of the structural state of charge at 0.9 L for the two electrode porosities depending on the SoC_{cell}.

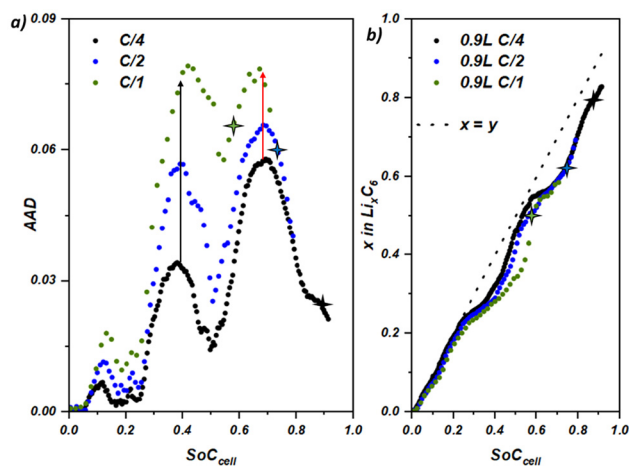


Fig. 11 Evolution of the structural state of charge dispersion for the 50% porosity graphite electrode at different cycling rates. (a) Evolution of the AAD parameter as a function of SoC_{cell} for different cycling rates. (b) Structural state of charge evolution as a function of SoC_{cell} at the 0.9 L position (near the current collector) for different cycling rates.

increasing the C-rate, which reflects the difficulty in homogenizing the lithium content along the electrode thickness. The increase in the AAD parameter as a function of the cycling rate is larger for the second bell-shaped curve (shown by a black arrow) than the last one (shown by a red arrow), meaning that the graphite electrode power ability seems to be more C-rate dependent from 0.25–0.6 SoC_{cell} than above. The evolution of x in Li_xC₆ at the 0.9 L position (near the current collector) was plotted and is shown in Fig. 11b as a function of the applied C-rate. By increasing the cycling rate, one can observe a structural state of charge being more and more delayed by deviating from the straight line in the region 0.25–0.6 cell SoC_{cell} (this is true for C/4 and C/2 rates that are in CC mode, whereas at the C/1 rate the cell entered the CV mode at ~0.55 SoC_{cell}). One interesting feature to note is that when the structural state is

above $x = 0.55$ (at the potential step between stage II formation and stage I formation), no additional delay is observed by increasing the C-rate. This highlights the lower dependence on the C-rate increase in this region of SoC_{cell} ($x > 0.55$). The data for the electrode with 30% porosity are provided in Note 9 (SI) and present very similar behaviour as for the electrode with 50% porosity.

We demonstrated here the detrimental impact of the high ionic tortuosity in the through-plane direction of graphite electrodes with flake particle shape, despite having almost 100% of interconnected porosity, indicating no problem of wetting in the electrode depth. The limited penetration depth of lithium ions through the electrode microstructure during fast lithiation generates depletions of salt concentration that appear upon charging, and it implies a current distribution that should be heterogeneous along the electrode thickness. We further analysed the local current distribution for the electrode porosity of 30%. By plotting the differential evolution of x in Li_xC₆ as a function of the electrochemical SoC_{cell} for each z -position (Fig. 6c and d), we determined the equivalent current of lithiation (effective C-rate) along the electrode thickness. The effective C-rate corresponds to the rate of structural state of charge evolution for a given scanned position and state of charge as a function of the global cell state of charge. Physically, it is an estimation of the lithiation rate, determined through the structural variations of the graphite particles. However, this is an estimation of the current only responsible for lithium intercalation and does not consider eventual secondary reactions such as SEI formation. Fig. 12 shows the evolution of the effective C-rate for the graphite electrode with 30% porosity, at the z -positions 0.1 L (near the separator) and 0.9 L (near the current collector), for the three applied C-rates. All the other positions from 0.1 L to 0.9 L recorded at a rate of C/4 are provided in Note 10 (Fig. S13). With this representation, we can easily observe that the distribution of current is favoured near the separator. As an example, looking at Fig. 12a around 0.1 SoC_{cell}, the 0.1 L position is in a higher regime of



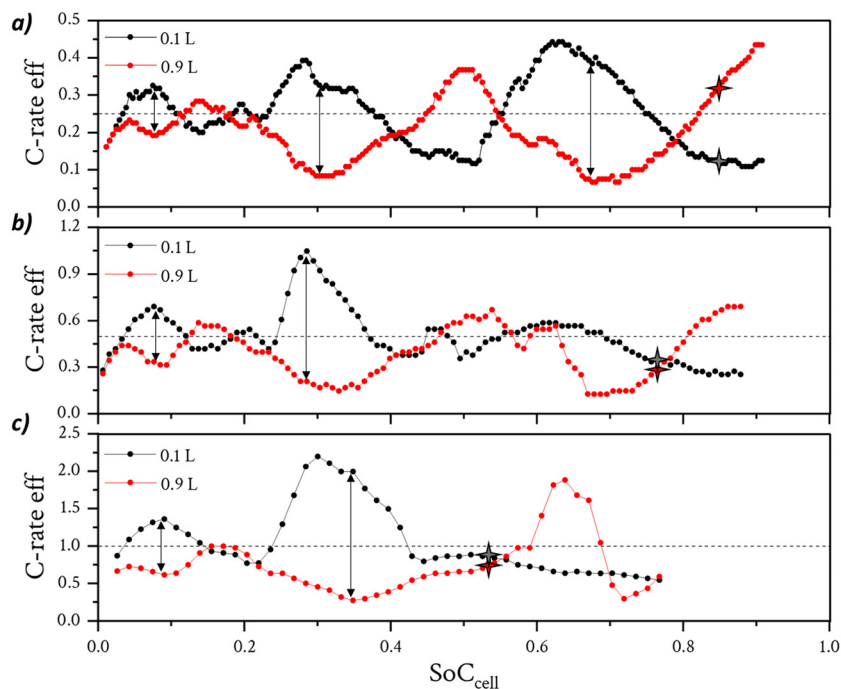


Fig. 12 Evolution of effective C-rates as a function of SoC_{cell} at the positions 0.1 L and 0.9 L (black and red curves, respectively) for the graphite electrode with 30% porosity. (a) Cycling rate of C/4; the dashed line at 0.25 corresponds to the applied C-rate at the cell level. (b) Cycling rate of C/2. (c) Cycling rate of C/1. The double arrows highlight the regions where electrons are distributed in priority near the separator/electrode interface. The switch between CC and CV periods is indicated by the grey stars.

lithiation exceeding the applied C-rate (0.25, C/4) while the 0.9 L position displays a lower regime of lithiation. In contrast, at other times of the cell lithiation (0.5 SoC_{cell} for example), the effective C-rate is higher for the 0.9 L position and the 0.1 L position displays a lower-regime of lithiation. With this, we observed opposite trends for the two curves, and this is in agreement with the behaviour described above. During the two-phase transitions (potential plateaus) the current is distributed where the resistance is the lowest and then near the separator because of a higher local salt concentration. This corresponds to a mass-transport limited period. Once the graphite particles near the separator exit the potential plateau, an extra resistance appears due to the decrease in the electrochemical potential, which redistributes the current to the delayed regions still present in the potential plateau (near the current collector). This corresponds to a period combining mass-transport limitation and an extra potential resistance limitation. This specific trend is repeated along the cell lithiation because of the several plateaus of potential that graphite undergoes, and this explains the opposite trends of effective C-rates near the separator and the current collector observed in Fig. 12. In addition, we noticed that the maximal effective C-rate reached (between 0.1 L and 0.9 L) is around two times higher than the applied C-rate, regardless of the cycling rate. We observed that the mid-Z-position thickness experiences a lower amplification of the effective C-rate (~ 1.5 amplification compared to two times) (Note 10, Fig. S13). The same trend

was observed for the graphite electrode with 50% porosity, with similar maximal effective C-rates (Note 11, SI).

These current distributions through the electrode thickness raise important questions about aging. We expect higher degradation processes near the separator/electrode interface for at least two reasons: (i) graphite particles systematically reach higher SoC and then undergo higher volumetric changes that can be detrimental in long-term cycling; (ii) higher kinetics of lithiation are observed near the separator, that probably can increase the local temperature and degrade the electrolyte and/or the SEI.

Conclusion

Rate capability tests were performed on graphite electrodes of 50% and 30% porosity by varying the electrolyte's salt concentration, showing high power limitation for the electrode with 30% porosity. An in-depth morphological investigation, carried out using X-ray holotomography, reveals a high tortuosity pathway for the less porous electrode, indicating a probable ionic transport limitation. These results were correlated by *operando* X-ray diffraction performed in the z-profile of the electrode.

A gradient of lithiation was indeed highlighted from the separator/electrode interface to the current collector/electrode, validating a power limited by the transport of lithium ions



through the electrode microstructures. The analysis of lithiation heterogeneities using AAD revealed a peculiar dynamic depending on the mechanism of lithium insertion. Indeed, it was found that the electrode lithiation was only controlled by mass transport in the biphasic regions, whereas a chemical potential barrier exists during solid solution processes and takes precedence over the mass transport. With the analysis of structural evolution, we estimated the local effective C-rate as a function of the electrode depth. It was observed that local current values can reach two times the applied current, regardless of the electrode porosity.

These works highlight concerns about the ageing phenomenon for high-rate battery applications because of the local current reaching twice the applied current for a tortuous electrode. These results can serve as experimental data to compare with modelling, based on Newman's model as an example.

Conflicts of interest

The authors declare that they have no conflicts of interest.

Data availability

Data are available upon reasonable request. DOIs for large-scale facility measurements are indicated as a reference in the manuscript.

Supplementary information (SI) is available. See DOI: <https://doi.org/10.1039/d6eb00003g>.

Acknowledgements

This work was financed by the Region Auvergne Rhône-Alpes (Pack Ambition Recherche 2021 – Projet IsoBATT) as part of Corentin Renais's thesis. Beamtime at the ESRF was granted within the Battery Pilot Hub MA-4929 “Multi-scale Multi-techniques investigations of Li-ion batteries: towards a European Battery Hub”. The authors acknowledge the ID31 beamline (ESRF, Grenoble) and the scientists involved in the XRD experiments (MA-4929 and IH-MA-424). For the morphological analysis, the authors acknowledge the ID16B beamline (ESRF, Grenoble). The following DOI corresponds to the experimental data acquired during these beamtimes: <https://doi.org/10.15151/ESRF-ES-1053703088> (MA-4929), <https://doi.org/10.15151/ESRF-ES-1397321743> (IH-MA-424) and <https://doi.org/10.15151/ESRF-ES-1581887512> (MA-4929).

References

- 1 M. De Rosa, O. Afanaseva, A. V. Fedyukhin and V. Bianco, Prospects and Characteristics of Thermal and Electrochemical Energy Storage Systems, *J. Energy Storage*, 2021, **44**, 103443, DOI: [10.1016/j.est.2021.103443](https://doi.org/10.1016/j.est.2021.103443).
- 2 M. Singh, J. Kaiser and H. Hahn, Effect of Porosity on the Thick Electrodes for High Energy Density Lithium Ion Batteries for Stationary Applications, *Batteries*, 2016, **2**(4), 35, DOI: [10.3390/batteries2040035](https://doi.org/10.3390/batteries2040035).
- 3 D. Antartis, S. Dillon and I. Chasiotis, Effect of Porosity on Electrochemical and Mechanical Properties of Composite Li-Ion Anodes, *J. Compos. Mater.*, 2015, **49**(15), 1849–1862, DOI: [10.1177/0021998314568653](https://doi.org/10.1177/0021998314568653).
- 4 Y. Ji, Y. Zhang and C.-Y. Wang, Li-Ion Cell Operation at Low Temperatures, *J. Electrochem. Soc.*, 2013, **160**(4), A636–A649, DOI: [10.1149/2.047304jes](https://doi.org/10.1149/2.047304jes).
- 5 S. Schweidler, L. De Biasi, A. Schiele, P. Hartmann, T. Brezesinski and J. Janek, Volume Changes of Graphite Anodes Revisited: A Combined *Operando* X-Ray Diffraction and *In Situ* Pressure Analysis Study, *J. Phys. Chem. C*, 2018, **122**(16), 8829–8835, DOI: [10.1021/acs.jpcc.8b01873](https://doi.org/10.1021/acs.jpcc.8b01873).
- 6 C. Fongy, A.-C. Gaillot, S. Jouanneau, D. Guyomard and B. Lestriez, Ionic vs Electronic Power Limitations and Analysis of the Fraction of Wired Grains in LiFePO₄ Composite Electrodes, *J. Electrochem. Soc.*, 2010, **157**(7), A885, DOI: [10.1149/1.3432559](https://doi.org/10.1149/1.3432559).
- 7 C. Fongy, S. Jouanneau, D. Guyomard, J. C. Badot and B. Lestriez, Electronic and Ionic Wirings Versus the Insertion Reaction Contributions to the Polarization in LiFePO₄ Composite Electrodes, *J. Electrochem. Soc.*, 2010, **157**(12), A1347, DOI: [10.1149/1.3497353](https://doi.org/10.1149/1.3497353).
- 8 J. S. Newman and C. W. Tobias, Theoretical Analysis of Current Distribution in Porous Electrodes, *J. Electrochem. Soc.*, 1962, **109**(12), 1183, DOI: [10.1149/1.2425269](https://doi.org/10.1149/1.2425269).
- 9 M. Doyle, T. F. Fuller and J. Newman, Modeling of Galvanostatic Charge and Discharge of the Lithium/Polymer/Insertion Cell, *J. Electrochem. Soc.*, 1993, **140**(6), 1526–1533, DOI: [10.1149/1.2221597](https://doi.org/10.1149/1.2221597).
- 10 T. F. Fuller, M. Doyle and J. Newman, Simulation and Optimization of the Dual Lithium Ion Insertion Cell, *J. Electrochem. Soc.*, 1994, **141**(1), 1–10, DOI: [10.1149/1.2054684](https://doi.org/10.1149/1.2054684).
- 11 K. G. Gallagher, S. E. Trask, C. Bauer, T. Woehrle, S. F. Lux, M. Tschech, P. Lamp, B. J. Polzin, S. Ha, B. Long, Q. Wu, W. Lu, D. W. Dees and A. N. Jansen, Optimizing Areal Capacities through Understanding the Limitations of Lithium-Ion Electrodes, *J. Electrochem. Soc.*, 2016, **163**(2), A138–A149, DOI: [10.1149/2.0321602jes](https://doi.org/10.1149/2.0321602jes).
- 12 S. J. Tambio, F. Cadiou, E. Maire, N. Besnard, M. Deschamps and B. Lestriez, The Concept of Effective Porosity in the Discharge Rate Performance of High-Density Positive Electrodes for Automotive Application, *J. Electrochem. Soc.*, 2020, **167**(16), 160509, DOI: [10.1149/1945-7111/abcb42](https://doi.org/10.1149/1945-7111/abcb42).
- 13 N. Dufour, M. Chandesris, S. Geniès, M. Cugnet and Y. Bultel, Lithiation Heterogeneities of Graphite According to C-Rate and Mass-Loading: A Model Study, *Electrochim. Acta*, 2018, **272**, 97–107, DOI: [10.1016/j.electacta.2018.03.196](https://doi.org/10.1016/j.electacta.2018.03.196).
- 14 H. Gu, Mathematical Analysis of a Zn/NiOOH Cell, *J. Electrochem. Soc.*, 1983, **130**(7), 1459–1464, DOI: [10.1149/1.2120009](https://doi.org/10.1149/1.2120009).



- 15 J. I. G. Dawkins, I. Martens, A. Danis, I. Beaulieu, D. Chhin, M. Mirolo, J. Drnec, S. B. Schougaard and J. Mauzeroll, Mapping the Total Lithium Inventory of Li-Ion Batteries, *Joule*, 2023, 7(12), 2783–2797, DOI: [10.1016/j.joule.2023.11.003](https://doi.org/10.1016/j.joule.2023.11.003).
- 16 C. Hogrefe, T. Waldmann, M. B. Molinero, L. Wildner, P. Axmann and M. Wohlfahrt-Mehrens, Cross-Sectional In Situ Optical Microscopy with Simultaneous Electrochemical Measurements for Lithium-Ion Full Cells, *J. Electrochem. Soc.*, 2022, 169(5), 050519, DOI: [10.1149/1945-7111/ac6c57](https://doi.org/10.1149/1945-7111/ac6c57).
- 17 S. Kang, S. J. Yeom and H. Lee, Side-View Operando Optical Microscopy Analysis of a Graphite Anode to Study Its Kinetic Hysteresis, *ChemSusChem*, 2020, 13(6), 1480–1484, DOI: [10.1002/cssc.201903289](https://doi.org/10.1002/cssc.201903289).
- 18 K. P. C. Yao, J. S. Okasinski, K. Kalaga, I. A. Shkrob and D. P. Abraham, Quantifying Lithium Concentration Gradients in the Graphite Electrode of Li-Ion Cells Using Operando Energy Dispersive X-Ray Diffraction, *Energy Environ. Sci.*, 2019, 12(2), 656–665, DOI: [10.1039/C8EE02373E](https://doi.org/10.1039/C8EE02373E).
- 19 S. Tardif, N. Dufour, J.-F. Colin, G. Gébel, M. Burghammer, A. Johannes, S. Lyonnard and M. Chandesris, Combining Operando X-Ray Experiments and Modelling to Understand the Heterogeneous Lithiation of Graphite Electrodes, *J. Mater. Chem. A*, 2021, 9(7), 4281–4290, DOI: [10.1039/D0TA10735B](https://doi.org/10.1039/D0TA10735B).
- 20 J. Landesfeind, J. Hattendorff, A. Ehrl, W. A. Wall and H. A. Gasteiger, Tortuosity Determination of Battery Electrodes and Separators by Impedance Spectroscopy, *J. Electrochem. Soc.*, 2016, 163(7), A1373–A1387, DOI: [10.1149/2.1141607jes](https://doi.org/10.1149/2.1141607jes).
- 21 G. Martínez-Criado, J. Villanova, R. Tucoulou, D. Salomon, J.-P. Suuronen, S. Labouré, C. Guilloud, V. Valls, R. Barrett, E. Gagliardini, Y. Dabin, R. Baker, S. Bohic, C. Cohen and J. Morse, ID16B: A Hard X-Ray Nanoprobe Beamline at the ESRF for Nano-Analysis, *J. Synchrotron Radiat.*, 2016, 23(1), 344–352, DOI: [10.1107/S1600577515019839](https://doi.org/10.1107/S1600577515019839).
- 22 P. Cloetens, W. Ludwig, J. Baruchel, D. Van Dyck, J. Van Landuyt, J. P. Guigay and M. Schlenker, Holotomography: Quantitative Phase Tomography with Micrometer Resolution Using Hard Synchrotron Radiation x Rays, *Appl. Phys. Lett.*, 1999, 75(19), 2912–2914, DOI: [10.1063/1.125225](https://doi.org/10.1063/1.125225).
- 23 A. Mirone, E. Brun, E. Gouillart, P. Tafforeau and J. Kieffer, The PyHST2 Hybrid Distributed Code for High Speed Tomographic Reconstruction with Iterative Reconstruction and a Priori Knowledge Capabilities, *Nucl. Instrum. Methods Phys. Res., Sect. B*, 2014, 324, 41–48, DOI: [10.1016/j.nimb.2013.09.030](https://doi.org/10.1016/j.nimb.2013.09.030).
- 24 A. Lyckegaard, G. Johnson and P. Tafforeau, Correction of Ring Artifacts in X-Ray Tomographic Images, *Int. J. Tomogr. Stat.*, 2011, 18, 1–9.
- 25 J. Schindelin, I. Arganda-Carreras, E. Frise, V. Kaynig, M. Longair, T. Pietzsch, S. Preibisch, C. Rueden, S. Saalfeld, B. Schmid, J.-Y. Tinevez, D. J. White, V. Hartenstein, K. Eliceiri, P. Tomancak and A. Cardona, Fiji: An Open-Source Platform for Biological-Image Analysis, *Nat. Methods*, 2012, 9(7), 676–682, DOI: [10.1038/nmeth.2019](https://doi.org/10.1038/nmeth.2019).
- 26 S. Berg, D. Kutra, T. Kroeger, C. N. Straehle, B. X. Kausler, C. Haubold, M. Schiegg, J. Ales, T. Beier, M. Rudy, K. Eren, J. I. Cervantes, B. Xu, F. Beuttenmueller, A. Wolny, C. Zhang, U. Koethe, F. A. Hamprecht and A. Kreshuk, Ilastik: Interactive Machine Learning for (Bio)Image Analysis, *Nat. Methods*, 2019, 16(12), 1226–1232, DOI: [10.1038/s41592-019-0582-9](https://doi.org/10.1038/s41592-019-0582-9).
- 27 J. Kieffer and J. P. Wright, PyFAI: A Python Library for High Performance Azimuthal Integration on GPU, *Powder Diffr.*, 2013, 28(S2), S339–S350, DOI: [10.1017/S0885715613000924](https://doi.org/10.1017/S0885715613000924).
- 28 The Matplotlib Development Team, *Matplotlib: Visualization with Python*, 2024. DOI: [10.5281/ZENODO.592536](https://doi.org/10.5281/ZENODO.592536).
- 29 M. Newville, T. Stensitzki, D. B. Allen and A. Ingargiola, *LMFIT: Non-Linear Least-Square Minimization and Curve-Fitting for Python*, 2014. DOI: [10.5281/ZENODO.11813](https://doi.org/10.5281/ZENODO.11813).
- 30 D. Erb, *Pybaselines: A Python Library of Algorithms for the Baseline Correction of Experimental Data*, 2024. DOI: [10.5281/ZENODO.5608581](https://doi.org/10.5281/ZENODO.5608581).
- 31 C. Heubner, C. Lämmel, A. Nickol, T. Liebmann, M. Schneider and A. Michaelis, Comparison of Chronoamperometric Response and Rate-Performance of Porous Insertion Electrodes: Towards an Accelerated Rate Capability Test, *J. Power Sources*, 2018, 397, 11–15, DOI: [10.1016/j.jpowsour.2018.06.087](https://doi.org/10.1016/j.jpowsour.2018.06.087).
- 32 S. R. Sivakkumar, J. Y. Nerkar and A. G. Pandolfo, Rate Capability of Graphite Materials as Negative Electrodes in Lithium-Ion Capacitors, *Electrochim. Acta*, 2010, 55(9), 3330–3335, DOI: [10.1016/j.electacta.2010.01.059](https://doi.org/10.1016/j.electacta.2010.01.059).
- 33 H. Buqa, D. Goers, M. Holzapfel, M. E. Spahr and P. Novák, High Rate Capability of Graphite Negative Electrodes for Lithium-Ion Batteries, *J. Electrochem. Soc.*, 2005, 152(2), A474, DOI: [10.1149/1.1851055](https://doi.org/10.1149/1.1851055).
- 34 D. Lu, Y. Shao, T. Lozano, W. D. Bennett, G. L. Graff, B. Polzin, J. Zhang, M. H. Engelhard, N. T. Saenz, W. A. Henderson, P. Bhattacharya, J. Liu and J. Xiao, Failure Mechanism for Fast-Charged Lithium Metal Batteries with Liquid Electrolytes, *Adv. Energy Mater.*, 2015, 5(3), 1400993, DOI: [10.1002/aenm.201400993](https://doi.org/10.1002/aenm.201400993).
- 35 H. Fujimoto, T. Yamaki, K. Shimoda, S. Fujinami, T. Nakatani, G. Kano, M. Kawasaki, Z. Ogumi and T. Abe, Phase Diagram of Li-Graphite Intercalation Compound Formed by the Charge/Discharge Reaction in Li-Ion Battery, *J. Electrochem. Soc.*, 2022, 169(7), 070507, DOI: [10.1149/1945-7111/ac7e77](https://doi.org/10.1149/1945-7111/ac7e77).
- 36 S. Takagi, K. Shimoda, J. Haruyama, H. Kiuchi, K. Okazaki, T. Fukunaga, Z. Ogumi and T. Abe, Operando Structural Analysis of Phase Transition of Graphite Electrode during Li De-Intercalation Process Using Neutron and Synchrotron Radiation X-Ray Diffraction, *Carbon*, 2023, 215, 118414, DOI: [10.1016/j.carbon.2023.118414](https://doi.org/10.1016/j.carbon.2023.118414).
- 37 L. E. Camacho-Forero, T. W. Smith and P. B. Balbuena, Effects of High and Low Salt Concentration in Electrolytes at Lithium-Metal Anode Surfaces, *J. Phys. Chem. C*, 2017, 121(1), 182–194, DOI: [10.1021/acs.jpcc.6b10774](https://doi.org/10.1021/acs.jpcc.6b10774).
- 38 M. Nie and B. L. Lucht, Role of Lithium Salt on Solid Electrolyte Interface (SEI) Formation and Structure in Lithium Ion Batteries, *J. Electrochem. Soc.*, 2014, 161(6), A1001–A1006, DOI: [10.1149/2.054406jes](https://doi.org/10.1149/2.054406jes).



- 39 M. Hao, S. Weng, C. Zhong, Y. Li and X. Wang, Structure and Evolution of Solid Electrolyte Interphase (SEI) at the Electrode-Electrolyte Interface, *Mater. Today Energy*, 2025, **53**, 101998, DOI: [10.1016/j.mtener.2025.101998](https://doi.org/10.1016/j.mtener.2025.101998).
- 40 S. Malifarge, B. Delobel and C. Delacourt, Determination of Tortuosity Using Impedance Spectra Analysis of Symmetric Cell, *J. Electrochem. Soc.*, 2017, **164**(11), E3329–E3334, DOI: [10.1149/2.0331711jes](https://doi.org/10.1149/2.0331711jes).
- 41 J. Landesfeind, M. Ebner, A. Eldiven, V. Wood and H. A. Gasteiger, Tortuosity of Battery Electrodes: Validation of Impedance-Derived Values and Critical Comparison with 3D Tomography, *J. Electrochem. Soc.*, 2018, **165**(3), A469–A476, DOI: [10.1149/2.0231803jes](https://doi.org/10.1149/2.0231803jes).
- 42 N. A. Zacharias, D. R. Nevers, C. Skelton, K. Knackstedt, D. E. Stephenson and D. R. Wheeler, Direct Measurements of Effective Ionic Transport in Porous Li-Ion Electrodes, *J. Electrochem. Soc.*, 2013, **160**(2), A306–A311, DOI: [10.1149/2.062302jes](https://doi.org/10.1149/2.062302jes).
- 43 Y. Guo, X. Li, Q. Qin, Z. Wang, H. Guo, J. Wang and G. Yan, Determination of the Tortuosity and Contact Resistances in Thick Graphite Anodes via Electrochemical Impedance Spectroscopy, *J. Power Sources*, 2023, **569**, 233003, DOI: [10.1016/j.jpowsour.2023.233003](https://doi.org/10.1016/j.jpowsour.2023.233003).
- 44 M. Kroll, D. Hlushkou, S. Schlabach, A. Hölzel, B. Roling and U. Tallarek, Reconstruction–Simulation Approach Verifies Impedance-Derived Ion Transport Tortuosity of a Graphite Battery Electrode, *J. Electrochem. Soc.*, 2018, **165**(13), A3156–A3163, DOI: [10.1149/2.0711813jes](https://doi.org/10.1149/2.0711813jes).
- 45 B. Tjaden, D. P. Finegan, J. Lane, D. J. L. Brett and P. R. Shearing, Contradictory Concepts in Tortuosity Determination in Porous Media in Electrochemical Devices, *Chem. Eng. Sci.*, 2017, **166**, 235–245, DOI: [10.1016/j.ces.2017.03.051](https://doi.org/10.1016/j.ces.2017.03.051).
- 46 S. J. Cooper, A. Bertei, P. R. Shearing, J. A. Kilner and N. P. Brandon, TauFactor: An Open-Source Application for Calculating Tortuosity Factors from Tomographic Data, *SoftwareX*, 2016, **5**, 203–210, DOI: [10.1016/j.softx.2016.09.002](https://doi.org/10.1016/j.softx.2016.09.002).
- 47 C. Renais, M. Mirolo, M. Servajon, J. Drnec, F. Alloin and C. Villevieille, Understanding Fast Charging Ability Limitation in Graphite Electrode for Li-Ion Batteries: Quasi-Thermodynamic Approach and Methodology, *Chem. Mater.*, 2025, **37**(15), 5647–5657, DOI: [10.1021/acs.chemmater.5c00722](https://doi.org/10.1021/acs.chemmater.5c00722).
- 48 C. Renais, B. Mercier-Guyon, D. Wasylowski, M. Sonnet, P. Dechent, M. Servajon, N. Blanc, S. Lyonnard, D. U. Sauer and C. Villevieille, Exploring Electrochemical Dynamics in graphite||LiNi0.8Mn0.1Co0.1O2 Cells via Operando Ultrasound and Multiprobe Approaches, *Nat. Commun.*, 2025, **16**(1), 7774, DOI: [10.1038/s41467-025-62935-z](https://doi.org/10.1038/s41467-025-62935-z).

